Insight from X-ray Absorption Spectroscopy to Octahedral/Tetrahedral Site Distribution in Sm-Doped Iron Oxide Magnetic Nanoparticles

M. A. Soldatov,[*,†] J. Göttlicher,[‡] S. P. Kubrin,[§] A. A. Guda,[†] T. A. Lastovina,[†] A. L. Bugaev,[†] Yu. V. Rusalev,[†] A. V. Soldatov,[†] and C. Lamberti[†,∥]

[†]The Smart Materials Research Center, Southern Federal University, Sladkova Street 174/28, 344090 Rostov-on-Don, Russia

[‡]Institute for Photon Science and Synchrotron Radiation (IPS), Karlsruhe Institute of Technology (KIT), Herman-von-Helmholtz-Platz 1, 76344 Eggenstein-Leopoldshafen, Germany

[§]Research Institute of Physics, Southern Federal University, Stachki Avenue 194, 344090 Rostov-on-Don, Russia

[∥]Department of Physics, NIS Interdepartmental Center and CrisDi Centre for Crystallography, University of Turin, via Giuria 1, 10125 Turin, Italy

S *Supporting Information*

ABSTRACT: A set of Sm-doped iron oxide magnetic nanoparticles (Fe$_x$O$_y$ NPs) of different sizes as an example of ferromagnetic NPs at room temperature was synthesized by microware-assisted methods. Powder X-ray diffraction and transmission electron microscopy showed Fe$_x$O$_y$ NPs with an inverse spinel structure. Mössbauer and X-ray absorption spectroscopy (XAS) were used to study the local atomic and electronic structure of iron in the NPs. Linear combination of XAS spectra of reference iron oxides failed in reproducing the spectra of Fe$_x$O$_y$ NPs [Piquer, C.; et al. *J. Phys. Chem. C* 2014, 118, 1332−1346]. We attribute this fact to the nonstoichiometric distribution of tetrahedral, T$_d^{3+}$, and octahedral, O$_h^{3+}$ and O$_h^{2+}$, sites in NPs compared to bulk references. This distribution was successfully reproduced by linear combination of theoretical XAS spectra obtained for clusters where iron was in T$_d^{3+}$, O$_h^{3+}$, and O$_h^{2+}$ defined oxidation and symmetry states. This approach allowed us to obtain the quantitative speciation of the fraction of T$_d^{3+}$, O$_h^{3+}$, and O$_h^{2+}$ sites as a function of the different size of the Sm-doped Fe$_x$O$_y$ NPs based on the XAS data. In contrast to the standard XAS reference compounds analysis where experimental spectra fits are limited to constant T$_d^{3+}$/O$_h^{3+}$ and T$_d^{3+}$/O$_h^{3+}$/O$_h^{2+}$ ratios and to Mössbauer spectroscopy that requires liquid helium temperatures, the proposed method opens a new possibility to quantitatively estimate the amount of each independent inequivalent iron site in terms of symmetry and oxidation state at room temperature.

1. INTRODUCTION

Small Fe$_x$O$_y$ nanoparticles (NPs) have demonstrated their unique properties for biomedical applications,[2] as contrast agents for magnetic resonance tomography,[3,4] carriers for target drug delivery, and active centers for hyperthermia.[5−7] Rare earth doping improves the magnetic properties of the NPs. The Gd-doped Fe$_x$O$_y$ NPs showed higher values of the specific power absorption rate compared to the superparamagnetic undoped samples,[8] whereas Eu- and Sm-doped Fe$_x$O$_y$ NPs were ferromagnetic even at room temperature.[9] Both bulk strain effects[10] and surface characteristics[11] have a strong influence on the magnetic properties of NPs. Proper surface functionalization ensures biocompatibility and stability[12] because uncoated magnetite Fe$_3$O$_4$ can be easily oxidized, generally resulting in the loss of magnetism and dispersibility. The oxidation state of surface iron atoms influences the cytotoxicity of the NPs.[13] The

latter work reports no apparent cytotoxicity for chemically stable γ-Fe$_2$O$_3$, whereas NPs containing ferrous and zerovalent iron were cytotoxic. The effect can be related to the generation of reactive oxygen species or to the strong affinity of the NPs for the cell membrane.[14]

In vitro characterization of the structural dynamics of Fe$_x$O$_y$ NPs in cells and tissues could be a crucial step to understand the origin of Fe$_x$O$_y$ NPs toxicity in biomedical applications. Such studies could significantly benefit from the method addressing the nonstoichiometry and Fe sites speciation in Fe$_x$O$_y$ NPs. Whereas room temperature could be essential for in vitro studies, spatial distribution could give additional

information on the origin of Fe_xO_y NPs toxicity in different cell compartments. The X-ray absorption near edge structure (XANES) spectroscopy is an appropriate tool that can be extended from the usual macroscopic XANES to μ-XANES that is capable of studying the distributions of NPs in the cells and tissues and of fine analysis of structural dynamics.

Proper phase characterization of the small Fe_xO_y NPs at room temperature is a challenging task. Magnetite and maghemite have similar magnetic values of 90 and 83.5 emu/g, respectively, which make it difficult to distinguish these two phases by magnetic characterization.[15] When dealing with crystalline materials, the X-ray diffraction (XRD) is generally applied as the most common method. However, having a cubic spinel-type crystal structure with similar cell parameters,[16−18] magnetite and maghemite NPs cannot be distinguished from each other by standard X-ray diffraction technique; the correlation between their diffraction profiles is higher than 99%.[19] In some cases, more complex analysis of diffraction data allows obtaining additional information on the size and shape of the NPs by using a pair distribution function approach.[20]

Complementary techniques are being applied for phase discrimination in Fe_xO_y NPs. Raman spectroscopy,[21] Fourier transform infrared spectroscopy,[9,21−23] and X-ray photo-electron spectroscopy[24,25] are among them. A number of studies shows the advantages of Mössbauer spectroscopy in distinguishing magnetite and maghemite phases.[11,26−29] XANES technique, being sensitive to the oxidation state of the absorbing element in general[30−37] and Fe in particular,[38,39] can be applied to distinguish magnetite from maghe-mite,[20,40−43] both of which have iron atoms in the average oxidation state of 2.67 and 3, respectively. The corresponding XANES spectra of these phases differ in the energy of the absorption edge by about 2 eV and in the intensity of the white line.[41] However, a more detailed analysis of the XANES data[1] shows that a linear combination of two bulk phases cannot be an adequate approach for modeling the structure of small NPs. In the present work, the Sm-doped Fe_xO_y NPs have been chosen as an example for particles with ferromagnetic properties at room temperature that are under discussion for medical applications. We use the local atomic probes for the characterization of Sm-doped Fe_xO_y NPs with different sizes, including XANES and Mössbauer spectroscopy. These methods were successfully applied together to analyze the local atomic and electronic structures of Fe.[44,45] Using theoretical simulations, we extend the analytical power of the method toward concentration of given iron positions in the sample, including Fe^{2+} and Fe^{3+} in T_d and O_h coordination. This approach is more appropriate for small NPs, which cannot be described as a superposition of crystalline phases of iron oxide references.

2. EXPERIMENTAL AND THEORETICAL METHODS

Ethylene glycol, $SmCl_3$, $FeCl_3$, NaOH, poly(ethylene glycol), and triethylene glycol (all Sigma-Aldrich) were used as starting substances. Three Sm^{3+}-doped materials were prepared via microwave-assisted (MW) polyol method by the following procedure: $FeCl_3$ (0.4 mM) and $SmCl_3$ (12.47 μmol) were dissolved in glycol. Then, 1 M glycol NaOH solution was added. The solution was purged with argon for 10 min. The mixture was heated in a MW reactor (Discover SP, CEM) for 1.5 h at 220 °C. After cooling to room temperature, the black precipitate was washed several times with ethanol and deionized water and collected with a magnet. The suspension

was treated in a vacuum oven at 50 °C to give a dry powder. The samples prepared using ethylene glycol, poly(ethylene glycol), and triethylene glycol are named in the following as samples I, II, and III, respectively. Sample IV was prepared by modified microwave-assisted co-precipitation in organic media as described elsewhere.[46,47]

Transmission electron microscopy (TEM) images were acquired using a G2 Spirit BioTWIN (Tecnai) microscope operated at an accelerating voltage of 80 kV. The X-ray diffraction (XRD) patterns were obtained using a Bruker D2 Phaser with Cu Kα-radiation (λ = 1.5418 Å). The Scherrer formula ($p = \frac{K \times \lambda}{\cos\theta \times b}$, where p is an estimated crystalline size, K = 0.92 is the Scherrer constant for spherical particles, λ is the wavelength of the radiation, θ is the Bragg angle, and b is the additional contribution to the integral broadening in radians)[48−50] was applied to the 220, 311, 400, 422, 511, and 440 reflections on the XRD patterns to estimate crystallite sizes. The Fe K- and Sm L_3-edge XANES spectra were measured at the SUL-X beamline (ANKA),[51] where the Si(311) double crystal monochromator was preferred to the Si(111) equivalent to increase the energy resolution. All the measurements were performed under air conditions at room temperature. The standard data reduction was performed using the Athena code.[52] A detailed description of the measurement conditions is given in the Supporting Information.

The magnetic properties of the samples were measured at room temperatures by a LakeShore vibrating sample magneto-meter model 7400. The Mössbauer spectra of synthesized iron oxide powder samples were acquired with a MS1104Em spectrometer equipped with a helium cryostat CCS-850. ^{57}Co isotope in a Cr matrix was used as a source of γ-radiation. Quantitative analysis of the spectra was performed using a SpectrRelax software.[53] The isomer shifts were determined relative to metallic α-Fe.

The XANES simulations have been performed by means of the finite difference method implemented within a FDMNES program package.[54−56] The radius of the cluster for calculation was equal to 7 Å and 0.2 Å interpoint distance was used for the grid construction. The atomic structure for different Fe sites was taken from the crystallographic data without further modifications. The finite difference method is a reliable approach to simulate XANES above the 3d metal K-edges, but it relies on the one-electron approximation. The crystal field splitting can be properly accounted in the one-electron approach,[57] but not the absolute energy position and multiplet effects in the localized 3d shell.[58] Therefore, we have intentionally excluded the pre-edge region from the comparison between theory and experiment and the fit index was calculated for the energy range 7120−7160 eV (Figures S2 and S3 marked by light green).

3. RESULTS AND DISCUSSION

The influence of the length of polyol chain on the particle size and mechanism of the NPs formation and growth is still poorly understood. However, the choice of the type of polyol is a critical to obtain well-defined NPs with the desired diameter and a narrow particle size distribution.[59] Formation of the magnetite phase occurs in the process of particular reduction of Fe^{3+} to Fe^{2+} by polyol molecules and successive co-precipitation reaction in the alkaline media.[60]

3.1. Transmission Electron Microscopy and X-ray Diffraction. The TEM images of the as-synthesized Sm-
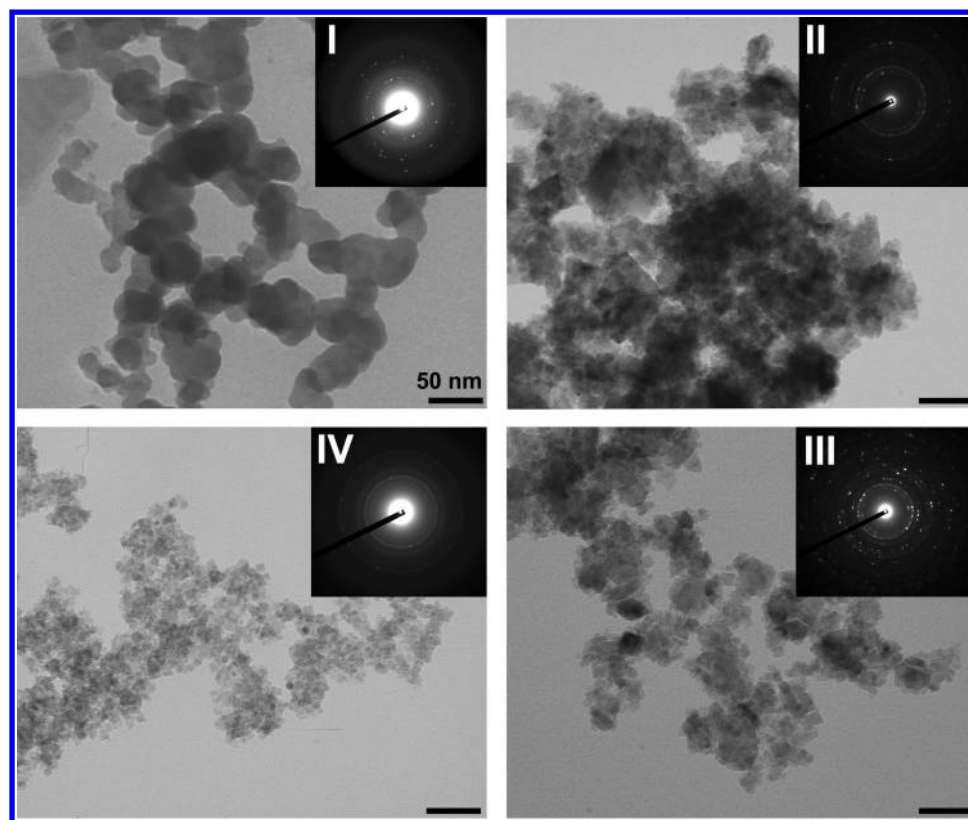
Figure 1. TEM image for Sm@Fe$_x$O$_y$ NPs samples I−IV. Scale bar is 50 nm. The insets report the corresponding electron diffraction pattern.

doped Fe$_x$O$_y$ NPs were used to calculate the particle sizes, and show a decreasing size of the NPs from samples I−IV, with samples II and III having similar particle sizes (Figure 1). The X-ray diffraction (XRD) measurements were performed for all the samples to confirm the crystalline structure of the formed NPs. The XRD patterns (Figure S1) demonstrate an inverse spinel structure. All the peaks are indexed to cubic Fe$_3$O$_4$ and γ-Fe$_2$O$_3$. No FeO and α-Fe$_2$O$_3$ peaks are found in the XRD patterns, indicating that all the samples have a Fe$_3$O$_4$/γ-Fe$_2$O$_3$ structure. Table 1 shows the average crystalline size obtained by

Table 1. Average Crystal Size Estimation[a]

	XRD crystal size (nm)	TEM (nm)
sample I	∼20	28.6 ± 12.4
sample II	∼14	13.7 ± 5.2
sample III	∼15	14.6 ± 4.3
sample IV	∼7	7.4 ± 1.4

[a]Second column: average particle size determined by applying the Scherrer equation to different Bragg reflections. Third column: mean value and the corresponding half-width at half-maximum of the particle size distribution determined in the TEM study.

the TEM statistics and by applying the Scherrer formula to the XRD patterns. It is clearly seen from both methods that the largest NPs (sample I, size above 20 nm) were synthesized using the shortest polyol chain; NPs synthesized using longer polyol chains—poly(ethylene glycol) (sample II) and tri-ethylene glycol (sample III)—showed an average size of about 15 nm. The results of the polyol synthesis are compared with modified microwave-assisted co-precipitation synthesis in the organic media. In the latter approach, an average size of NPs was 7 nm (sample IV).

3.2. Mössbauer Spectroscopy. The iron oxide NPs exhibit a superparamagnetic behavior, i.e., its magnetization vector can spontaneously reverse the orientation.[61] The relaxation time has an exponential temperature dependence $\tau_r = \tau_0 e^{KV/k_B T}$, where τ_0 is typically in the range $10^{-9}-10^{-12}$ s, K is the magnetic anisotropy constant, V is the particle volume, k_B is the Boltzmann's constant, and T is the temperature. Below the so-called blocking temperature (T_B), when τ_r is long compared to the Mössbauer measurement time (τ_m), the magnetically split spectra are obtained.[62−64] Above T_B, the magnetic structure of Mössbauer spectrum collapses into two paramagnetic lines. Moreover, the magnetic hyperfine field values H decrease much faster with increasing temperature.[64] This phenomenon is explained by thermally excited oscillations of magnetization around an energy minimum. The collective magnetic excitations due to superparamagnetic relaxation can be described by $H(T) = H_0\left(1 - \frac{kT}{KV}\right)$, where H_0 is the hyperfine magnetic field at zero temperature and its value is usually taken as that of the bulk materials.[53] Thus, the superparamagnetism makes the identification of the iron oxide phase by means of Mössbauer spectroscopy at room temperature complicated, if not impossible. For example, the room-temperature Mössbauer spectra of hematite,[65] goethite, and maghemite[27] NPs <20 nm in size are the doublets with equal parameters.

Figure 2 shows the Mössbauer spectra for samples I−IV with parameters' sizes listed in Table 2. The spectrum of sample I consists of a doublet and three sextets. The doublet component is connected to superparamagnetic NPs whose phase cannot be revealed at room temperatures. The absence of Zeeman splitting of the doublet component is explained by super-paramagnetic properties of the NPs with sizes 5−20 nm.[11,27,66]
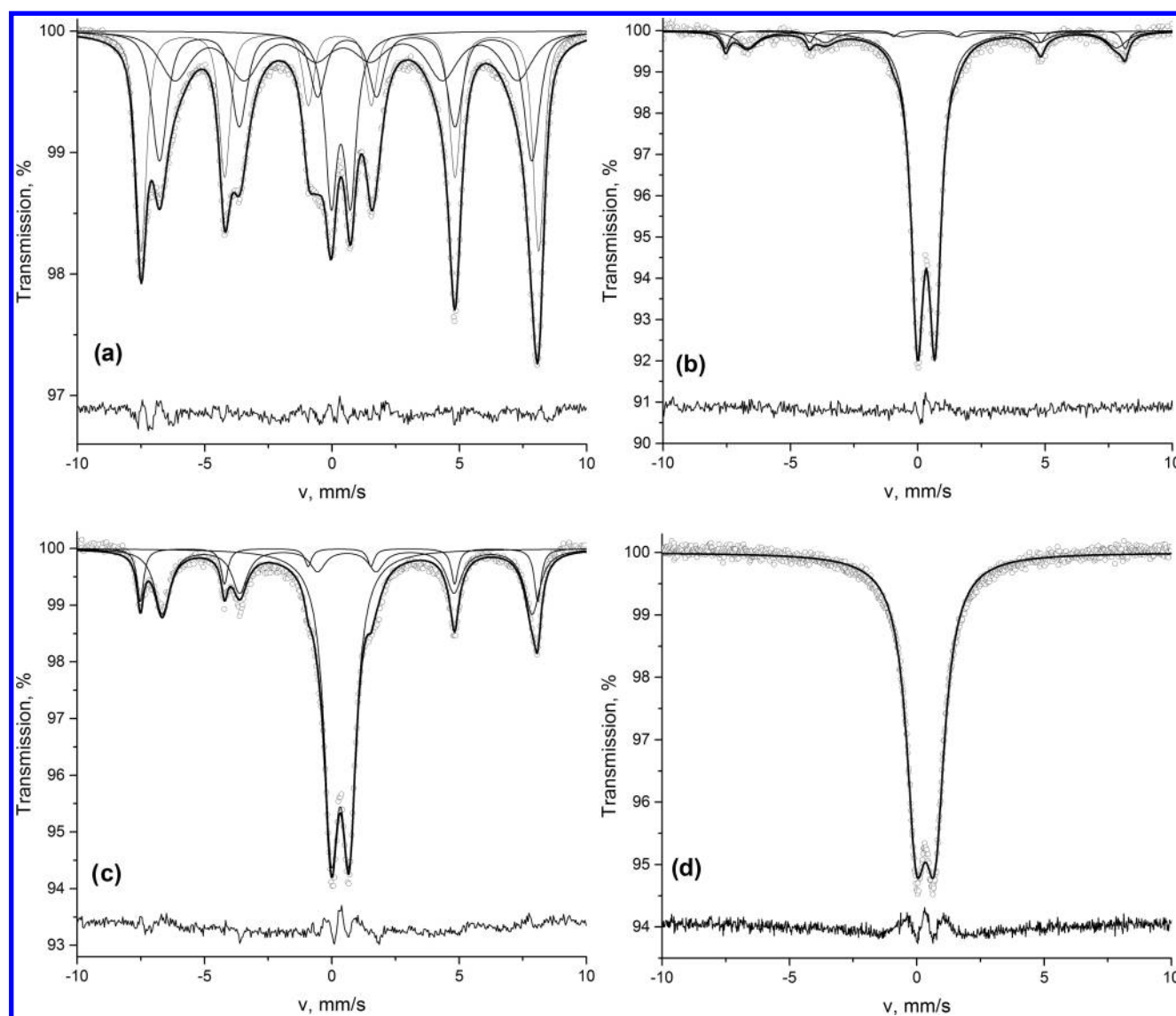
Figure 2. (a) Room-temperature experimental Mössbauer spectra (circles), fitted spectra (black curves) with individual contributions from different sextets and doublets (gray curves) and difference between theoretical and experimental spectra (black, curve) of sample I. (b−d) as (a) for samples II, III, and IV, respectively.

Table 2. Quantified Parameters of the Mössbauer Spectra[a]

samples	T (K)	component	$\delta \pm 0.02$ (mm/s)	$\varepsilon \pm 0.02$ (mm/s)	$H \pm 5$ (kOe)	$G \pm 0.02$ (mm/s)	$S \pm 5$ (%)	Fe state	χ^2
I	300	D	0.35	0.75		0.56	14	SPM	3.088
		S1	0.31	0.01	484	0.52	33	T_d^{3+}	
		S2	0.56	−0.06	453	0.72	30	$O_h^{3+/2+}$	
		S3	0.50	0.12	417	1.39	24	$O_h^{3+/2+}$	
II	300	D	0.33	0.69		0.58	79	SPM	1.400
		S1	0.30	0.00	486	0.33	6	T_d^{3+}	
		S2	0.57	0.00	449	0.95	15	$O_h^{3+/2+}$	
III	300	D	0.33	0.70		0.68	58	SPM	4.923
		S1	0.30	−0.02	484	0.31	11	T_d^{3+}	
		S2	0.60	0.01	451	0.73	31	$O_h^{3+/2+}$	
IV	20	A1	0.43	−0.04	493	1.10	63	T_d^{3+}	2.811
		A2	0.47	0.01	519	0.72	37	O_h^{3+}	
IV	300	D	0.34	0.73		0.95	100	SPM	2.267

[a]δ—isomer shift, ε—quadrupole splitting, H—effective magnetic field on ^{57}Fe nuclei, G—linewidth, S—area of the components in spectrum, χ^2—Pearson's criteria, SPM—superparamagnetic phase.

The Zeeman sextets S1−S3 can be fitted with parameters close to the crystalline magnetite[67] and may be related to Fe T_d^{3+} and $O_h^{3+/2+}$ configurations. Thus, S1 corresponds to Fe^{3+} ions in a tetrahedral oxygen coordination. The S2 and S3 correspond to iron ions averaged due to Vervey exchange with a formal valence $Fe^{2.5+}$ in octahedral coordination. Different isomer shifts and effective magnetic fields in S2 and S3 sextets are explained by the fact that these sextets are related to NPs with different sizes.

Spectra for samples II and III were fitted with two Zeeman sextets S1 and S2 and a paramagnetic doublet. Similar to the previous discussion, the doublet component corresponds to the superparamagnetic NPs and the sextet components to Fe T_d^{3+} and $O_h^{3+/2+}$ configurations. However, the concentration of superparamagnetic NPs is higher than that in sample I. Mössbauer spectrum of sample IV at room temperature consists solely of a doublet related to the superparamagnetic NPs. Figure 3 shows a spectrum of the same sample measured
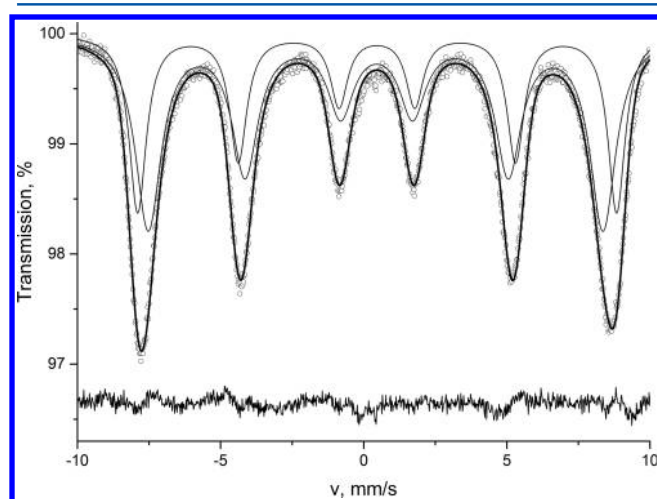

Figure 3. Mössbauer spectrum (circles), fit (curve) with individual contributions from different sextets (curves) for sample IV measured at 20 K.

at 20 K, which has already two Zeeman sextets. A1 sextet reveals a smaller isomer shift and corresponds to Fe T_d^{3+} and A2 sextet corresponds to Fe O_h^{3+}. Area of A1 component is almost twice as large as the area for A2 component. This fact is attributed to the high amount of Fe vacancies in B-position (magnetite has a typical spinel structure $A^{2+}B_2^{3+}O_4^{2-}$, where A positions have an octahedral coordination, whereas B position can be in both octahedral or tetrahedral coordinations; Figure 4a).[68] Moreover, isomer shifts for tetrahedral and octahedral environments of Fe^{3+} at 20 K are equal to 0.4 and 0.5 mm/s, respectively.[69] The isomer shift for octahedral A2 sextet is smaller, which is probably related to oxygen vacancy formation.

3.3. Fe K-Edge XANES Spectroscopy. The Sm L_2-edge that is only 200 eV above the Fe K-edge imposes obvious limitations on the Fe extended X-ray absorption fine structure (EXAFS) analysis for Sm-doped samples and restricts analysis to XANES part of the spectra. Figure 4b shows the Fe K-edge XANES spectra of samples I−IV, which are quite typical for inverse spinel Fe_xO_y NPs[1,70] and somehow are in between of reference spectra of bulk magnetite and maghemite (Figure 4c). The latter was attributed to a single-phase nonstoichiometric oxide with a cell parameter lying between the pure stoichiometric magnetite and maghemite.[1] There is an obvious

shift in the absorption edge to a higher energy in the spectrum of sample IV compared to the spectra of samples I−III, suggesting a higher average oxidation state of iron atoms in that sample, which can be connected to a higher surface-to-volume ratio in small NPs.

Linear combination fits were performed for the experimental spectra of samples I−IV using Fe_3O_4 and γ-Fe_2O_3 as references. The trend of higher amount of γ-Fe_2O_3 phase in smaller NPs is evident. However, the fit results are quantitatively worse than expected for a linear combination fit. We attribute this fact to a nonstoichiometric phase in Fe_xO_y NPs, making the bulk Fe_3O_4 and γ-Fe_2O_3 as references nonrepresentative models of the local environment of iron in our samples. Small Fe_xO_y NPs doped with rare earth elements have a high surface-to-volume ratio, which could destroy charge ordering. On the other hand, the oxidation rate of small Fe_xO_y NPs is quite high, leading to higher number of defects. Therefore, the model, which is appropriate for bulk samples, is not fully applicable for NPs. It has already been shown that the linear combination analysis is not valid for small iron oxide magnetic NPs.[1] To address this problem, we apply theoretical calculations to extract separate spectra for tetrahedral and octahedral sites of iron in magnetite and use them for the fitting.

The bulk structure of magnetite above Verwey transition is known for a period of more than a century;[71] however, a detailed information on the ground state of the low-temperature phase has been eluded.[72] After quite a number of studies,[73−79] a "trimeron"-based charge ordered structure with a number of inequivalent iron sites has been recently proposed.[80] For room-temperature experiments, we use a simple approximation with only three inequivalent sites of iron in the structure of bulk Fe_3O_4 and corresponding NPs: (i) Fe^{3+} with four oxygen neighbors in tetrahedral coordination (T_d^{3+}); (ii) Fe^{3+} with six oxygen neighbors in octahedral coordination (O_h^{3+}); and (iii) Fe^{2+} with six oxygen neighbors in octahedral coordination (O_h^{2+}). The fact of considering two different oxidation states is not trivial. At room temperature (above Verwey transition point), there is a fast charge hoping between octahedral sites. Therefore, the average oxidation state for iron in O_h position is expected to be $O_h^{2.5+}$, a fact observed in Mössbauer spectra. In contrast, Fe 1s core hole relaxation process is faster (10^{-15} s);[81] thus, for XANES spectroscopy, the model with two sites O_h^{3+}, O_h^{2+} is more preferable than $O_h^{2.5+}$. We consider that O_h^{3+}, O_h^{2+} sites have the same atomic structure, but due to different electronic configuration, the position of absorption edge of O_h^{3+} is shifted to higher energies (see Figure 4d).

The starting point of the analysis was a γ-Fe_2O_3 (maghemite). In this compound, the Fe ions occupy two inequivalent sites: T_d^{3+} and O_h^{3+}. Theoretical spectra simulated for tetrahedral and octahedral sites were summed up with a 1:1 ratio and energy position of the absorption edge was fitted (Figure 4c). The criteria for the quality of the fitting procedure was the R_{factor}, i.e., an integral over the XANES energy range (7120−7160 eV) of the squared difference between experimental spectrum and fit normalized by an integral of the squared experimental spectrum.

Then, the energy shifts for theoretical spectra of T_d^{3+} site were frozen and both O_h spectra were added into fitting procedure; however, the superposition was calculated for three spectra: T_d^{3+}:O_h^{3+}:O_h^{2+} with a weight coefficient 1:1:1 for the reference Fe_3O_4. Based on such a fit, a shift between O_h^{2+} and O_h^{3+} spectra was estimated, resulting in a relative energy shift of
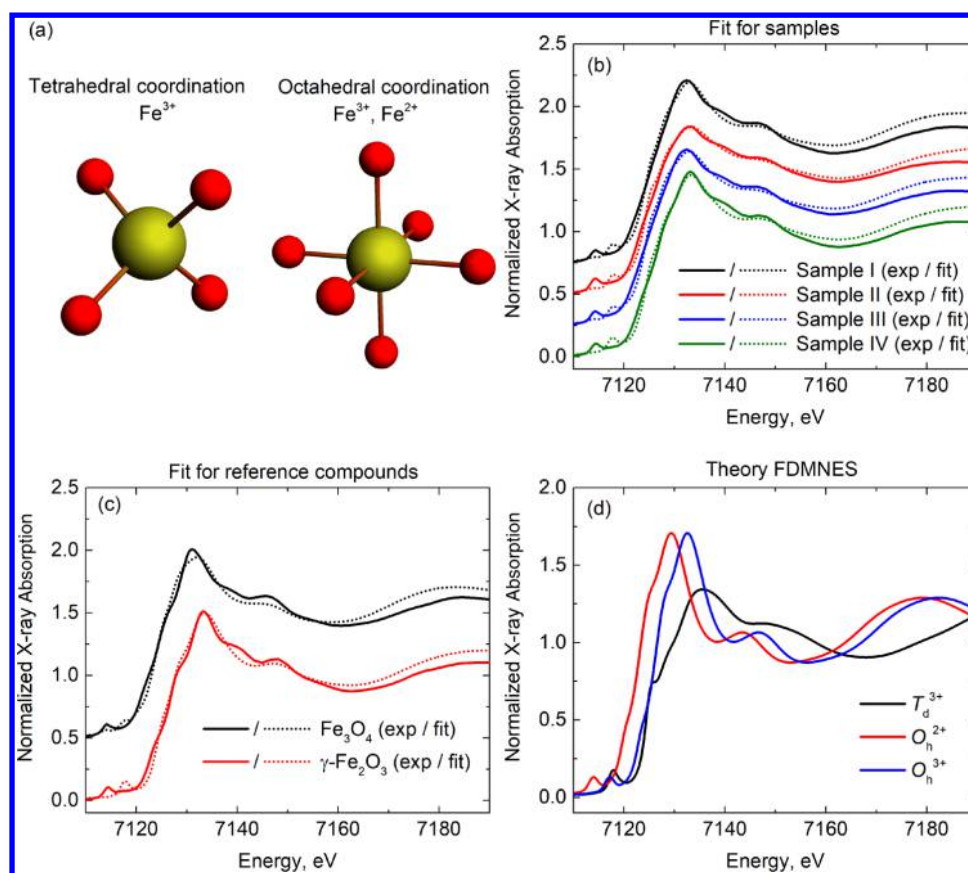
Figure 4. (a) Atomistic representation of tetrahedrally and octahedrally coordinated Fe ions. (b) Experimental and theoretical fit spectra samples I–IV. (c) Experimental and theoretical fit spectra for reference Fe_3O_4 and γ-Fe_2O_3 model compounds. (d) Theoretical spectra for T_d^{3+}, O_h^{3+}, and O_h^{2+} Fe sites, used in the fit procedures.

3.2 eV. Using such an approach, we deduced the theoretical XANES spectra and the chemical shift for three inequivalent Fe sites in inverse spinel iron oxide (Figure 4d). In the next step, the chemical shifts were fixed and the fitting procedure was to search the concentrations of inequivalent iron sites in samples I–IV. The results of inequivalent site concentration fit are compared to the XANES phase concentration fit and Mössbauer data (Figure 5). The Fe K-edge XANES phase concentration fits for samples I–IV are given in the Supporting Information.

The XANES experiment reference spectra linear combination fit is sensitive to γ-Fe_2O_3 and Fe_3O_4 phases. In this case, the inequivalent sites population is calculated taking into account that there are 1:1 T_d^{3+}/O_h^{3+} sites in ideal γ-Fe_2O_3 and 1:1:1 $T_d^{3+}/O_h^{3+}/O_h^{2+}$ sites in ideal Fe_3O_4, and thus the population of T_d^{3+} and O_h^{3+} configurations would be always equal. The XANES fit using experimental reference spectra is justified and well-working when the chosen references are representative of the iron spices present in the unknown material, otherwise they will fail or even provide misleading results. This can be the case for nonstoichiometric systems. Room-temperature Mössbauer spectroscopy for superparamagnetic NPs also has a limitation in differentiation of the charge state in the octahedral position. The approach that we suggest in this study is sensitive to both inequivalent atomic positions and charge states and could provide additional information on the inequivalent site populations.

Such an approach tends to show a higher tetrahedral site population for Fe_xO_y NPs compared to standard experimental
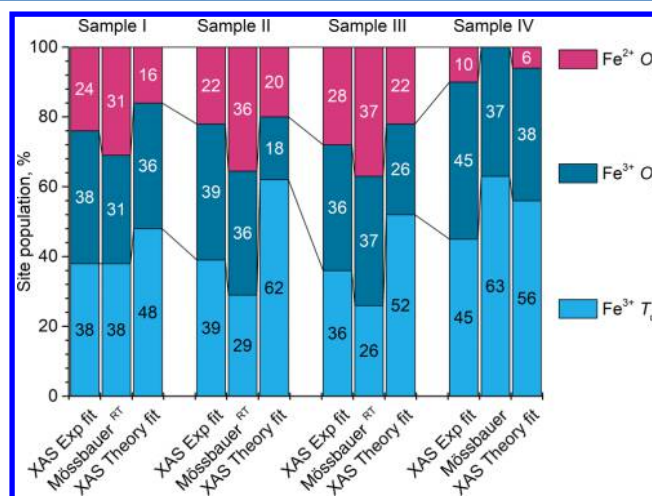

Figure 5. Population histogram of inequivalent sites of Fe in Fe_xO_y NPs based on results of XANES experiment reference fit, room-temperature Mössbauer for samples I–III, 20 K Mössbauer for sample IV and XANES theory fit.

reference spectra fit and room-temperature Mössbauer data. All the methods show an increase in the Fe oxidation state and in the amount of tetrahedral sites in small NPs.

3.4. Sm L$_3$-Edge XANES Spectroscopy. Figure 6 shows the experimental Sm L$_3$-edge XANES spectra for samples I–IV compared to reference Sm_2O_3. The spectra for all the samples are quite similar and reveal the Sm^{3+} oxidation state. However,
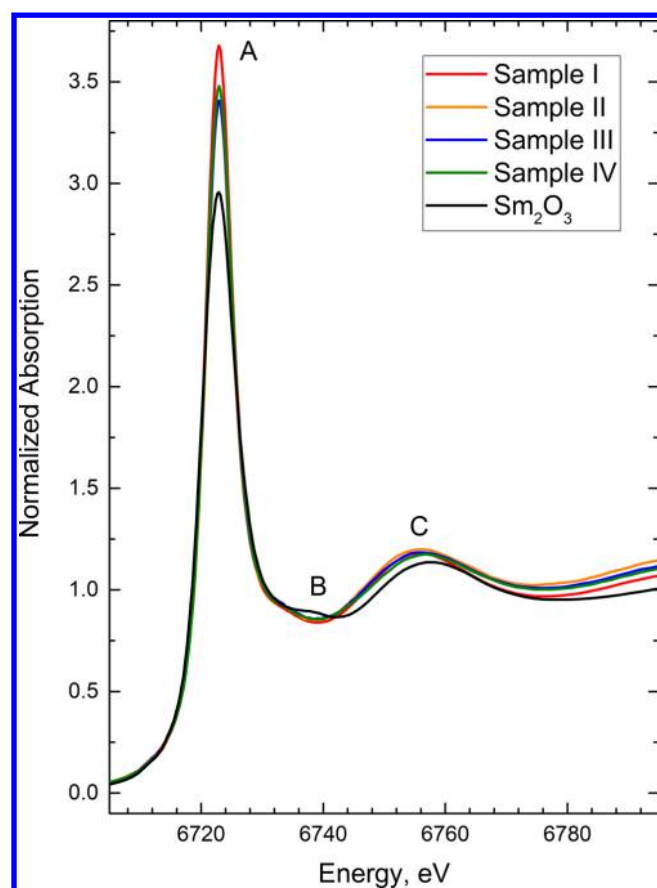
Figure 6. Experimental Sm L_3-edge XANES spectra of samples I–IV compared to reference Sm_2O_3.

there are some differences in the intensity of the white line peak A and a slight shift of peak C. The comparison of the series of XANES spectra collected for samples I–IV with that of Sm_2O_3 reference evidences three main peculiarities: (i) the increase in the white line intensity, (ii) the decrease in B peak intensity, and (iii) the red-shift of C peak accompanied by a slight increase in intensity. The oxidation state of Sm could be addressed based on the analysis of white line intensity. Indeed, the white line intensity increase is indicative of a higher oxidation state of the Sm atoms in NPs. Particularly, white line intensity for sample I is higher compared to other samples, which implies the higher oxidation state of the Sm in sample I. However, there is no straight correlation between the Fe and Sm oxidation states, as the white line intensities for samples II–IV are almost the same. The interplay of all the peaks intensities could be attributed to the phase composition changes. Peak C in the Sm-doped Fe_xO_y NPs samples is shifted in the energy relative to Sm_2O_3. According to the Natoli's rule,[82] the Sm–O distances in the Sm-doped Fe_xO_y NPs are thus larger than those in Sm_2O_3. However, a more quantitative EXAFS analysis of the Sm–O distances is not possible due to the overlapping of the EXAFS oscillations above Sm L_3-edge and Fe K-edge at 7112 eV, but qualitatively, the Fourier transformation using the EXAFS data up to k 8.5 shows Sm first shell peak positions for the samples at higher R values than for Sm_2O_3 (Figure S6, not phase corrected), hence in agreement with the conclusions from the shift of peak C. The higher Sm–O distance in the Sm Fe_xO_y NPs than in Sm_2O_3 (2.355 Å, 6-fold) compared with the average Sm–O of 2.491 Å of 8-fold Sm in samarium

orthoferrite ($SmFeO_3$) could indicate a higher Sm coordination also in the Fe_xO_y NPs (for more details see the Supporting Information).

Based on the reagent loading the Sm content should be about 5.5–5.7 wt %. If the content of Sm is in the range 5–10 wt %, Sm_2O_3 or $SmFeO_3$ mineral phases should have been detectable with the XRD as long as they are assumed to be crystalline. If no Sm_2O_3 or $SmFeO_3$ has been found with the XRD, then either the amounts of Sm mineral phases are too low, or they are not crystalline, or Sm is indeed absorbed or incorporated in the Fe_xO_y NPs. Because there are differences in the spectral shape of Sm L_3 spectra from NPs and Sm_2O_3, we would exclude that all the Sm is present as Sm_2O_3.

Specific absorption rate (SAR) is related to the heat losses of the Fe_xO_y NPs in alternate electromagnetic field. It is proportional to the hysteresis loop area of the magnetic nanoparticles.[83] Therefore, SAR can be improved by increasing the saturation magnetization (M_s) and the coercive field (H_c) of the magnetic nanoparticles. In general, the room-temperature saturation magnetization decreases along with nanoparticle size and is in general low for iron oxides, which makes the anisotropy variations for the nanoparticles a promising approach to increase the H_c value of the hysteresis loop and improve the SAR.[84]

By comparing the magnetic properties of the sample with the largest particles (sample 1) and smallest particles (sample 4), we see a change from ferromagnetic state to superparamagnetic state. The value of the H_c and M_r/M_s are close to the nano-octopods with similar size distribution.[84] This fact can be explained by the nonspherical shape of our nanoparticles, which increases the coercivity value from spherical ones.

Our results for the Fe^{3+}/Fe^{2+} distribution support Hiemstra's surface-depletion model in terms of the location of disorder and the variations of Fe^{2+} and Fe^{3+} occupancies with size, similar to ferrihydrite.[85]

4. CONCLUSIONS

A set of Sm-doped Fe_xO_y NPs of different size was synthesized by varying the polyol chain length in the microwave-assisted polyol method and compared to the small NPs synthesized by modified microwave-assisted co-precipitation in organic media. The XAS analysis confirmed the Sm^{3+} oxidation state in Sm-doped Fe_xO_y and elongated Sm–O distances compared to Sm_2O_3. The average oxidation state of iron in different samples was determined by means of standard linear combination fit of Fe K-edge XANES. We showed that the reconstruction of the XANES spectra using a linear combination of experimental spectra obtained from model compounds is a powerful technique to obtain a quantitative analytical speciation, which, however is not fully applicable for small NPs due to the nonstoichiometric concentration of tetrahedral and octahedral iron positions relative to bulk γ-Fe_2O_3 and Fe_3O_4 references. Therefore, another set of appropriate references should be used for the fit, which is not generally available. We showed that this drawback can be overcome using the theoretically calculated XANES spectra for specific octahedral and tetrahedral sites in Sm-doped Fe_xO_y NPs without restriction on their stoichiometry.

Quantification of the amount of Fe in $T_d^{3+}/O_h^{3+}/O_h^{2+}$ configurations was performed by means of two independent approaches—Mössbauer and theoretical calculation of Fe K-edge XANES. These methods show that the smallest NPs are oxidized stronger and all the NPs in general contain a larger

amount of tetrahedral Fe^{3+} sites compared to bulk Fe_3O_4. This amount of tetrahedral Fe^{3+} is underestimated by linear combination fit when bulk Fe_3O_4 and γ-Fe_2O_3 are used as references. Additionally, we showed the advantage of XAS over Mössbauer for in vitro studies that require room temperature.

The approach of quantifying the local atomic structure of nanoparticles, as we have demonstrated here for Sm-doped Fe_xO_y NPs by reproducing measured Fe K XANES with a linear combination of theoretical XAS spectra of clusters, is a promising procedure to improve the characterization of such particles. Further research on the development of nanoparticles with distinct properties for application in technology and medicine will benefit from this approach.

■ ASSOCIATED CONTENT

Ⓢ Supporting Information

The Supporting Information is available free of charge on the ACS Publications website at DOI: 10.1021/acs.jpcc.7b12797.

XRD data, Fe K-edge XANES fit and experiment details, Sm L_3-edge XAS details, magnetic measurements (PDF)

■ AUTHOR INFORMATION

Corresponding Author
*E-mail: mikhail.soldatov@gmail.com.

ORCID Ⓞ
M. A. Soldatov: 0000-0003-1918-7875
A. L. Bugaev: 0000-0001-8273-2560
C. Lamberti: 0000-0001-8004-2312

Notes
The authors declare no competing financial interest.

■ ACKNOWLEDGMENTS

■ REFERENCES

(1) Piquer, C.; Laguna-Marco, M. A.; Roca, A. G.; Boada, R.; Guglieri, C.; Chaboy, J. Fe K-Edge X-ray Absorption Spectroscopy Study of Nanosized Nominal Magnetite. *J. Phys. Chem. C* **2014**, *118*, 1332−1346.

(2) Pankhurst, Q. A.; Thanh, N. T. K.; Jones, S. K.; Dobson, J. Progress in Applications of Magnetic Nanoparticles in Biomedicine. *J. Phys. D: Appl. Phys.* **2009**, *42*, No. 224001.

(3) Thorek, D. L. J.; Chen, A. K.; Czupryna, J.; Tsourkas, A. Superparamagnetic Iron Oxide Nanoparticle Probes for Molecular Imaging. *Ann. Biomed. Eng.* **2006**, *34*, 23−38.

(4) Tong, S.; Hou, S.; Zheng, Z.; Zhou, J.; Bao, G. Coating Optimization of Superparamagnetic Iron Oxide Nanoparticles for High T_2 Relaxivity. *Nano Lett.* **2010**, *10*, 4607−4613.

(5) Deatsch, A. E.; Evans, B. A. Heating Efficiency in Magnetic Nanoparticle Hyperthermia. *J. Magn. Magn. Mater.* **2014**, *354*, 163−172.

(6) Berret, J. F.; Schonbeck, N.; Gazeau, F.; El Kharrat, D.; Sandre, O.; Vacher, A.; Airiau, M. Controlled Clustering of Superparamagnetic Nanoparticles Using Block Copolymers: Design of New Contrast Agents for Magnetic Resonance Imaging. *J. Am. Chem. Soc.* **2006**, *128*, 1755−1761.

(7) Tartaj, P.; Morales, M. A.; Veintemillas-Verdaguer, S.; González-Carreño, T.; Serna, C. J. The Preparation of Magnetic Nanoparticles for Applications in Biomedicine. *J. Phys. D: Appl. Phys.* **2003**, *36*, R182−R197.

(8) Drake, P.; Cho, H.-J.; Shih, P.-S.; Kao, C.-H.; Lee, K.-F.; Kuo, C.-H.; Lin, X.-Z.; Lin, Y.-J. Gd-Doped Iron-Oxide Nanoparticles for Tumour Therapy via Magnetic Field Hyperthermia. *J. Mater. Chem.* **2007**, *17*, 4914−4918.

(9) De Silva, C. R.; Smith, S.; Shim, I.; Pyun, J.; Gutu, T.; Jiao, J.; Zheng, Z. Lanthanide(III)-Doped Magnetite Nanoparticles. *J. Am. Chem. Soc.* **2009**, *131*, 6336−6337.

(10) Levy, M.; Quarta, A.; Espinosa, A.; Figuerola, A.; Wilhelm, C.; García-Hernández, M.; Genovese, A.; Falqui, A.; Alloyeau, D.; Buonsanti, R.; et al. Correlating Magneto-Structural Properties to Hyperthermia Performance of Highly Monodisperse Iron Oxide Nanoparticles Prepared by a Seeded-Growth Route. *Chem. Mater.* **2011**, *23*, 4170−4180.

(11) Tronc, E.; Ezzir, A.; Cherkaoui, R.; Chanéac, C.; Noguès, M.; Kachkachi, H.; Fiorani, D.; Testa, A. M.; Grenèche, J. M.; Jolivet, J. P. Surface-Related Properties of γ-Fe_2O_3 Nanoparticles. *J. Magn. Magn. Mater.* **2000**, *221*, 63−79.

(12) Wu, W.; He, Q.; Jiang, C. Magnetic Iron Oxide Nanoparticles: Synthesis and Surface Functionalization Strategies. *Nanoscale Res. Lett.* **2008**, *3*, 397−415.

(13) Auffan, M.; Achouak, W.; Rose, J.; Roncato, M.-A.; Chanéac, C.; Waite, D. T.; Masion, A.; Woicik, J. C.; Wiesner, M. R.; Bottero, J.-Y. Relation Between the Redox State of Iron-Based Nanoparticles and Their Cytotoxicity Toward *Escherichia coli*. *Environ. Sci. Technol.* **2008**, *42*, 6730−6735.

(14) Valdiglesias, V.; Kiliç, G.; Costa, C.; Fernández-Bertólez, N.; Pásaro, E.; Teixeira, J. P.; Laffon, B. Effects of Iron Oxide Nanoparticles: Cytotoxicity, Genotoxicity, Developmental Toxicity, and Neurotoxicity. *Environ. Mol. Mutagen.* **2015**, *56*, 125−148.

(15) Cullity, B. D.; Graham, C. D. *Introduction to Magnetic Materials*; John Wiley & Sons: Hoboken, NJ, 2011.

(16) Fleet, M. E. The Structure of Magnetite. *Acta Crystallogr., Sect. B: Struct. Sci., Cryst. Eng. Mater.* **1981**, *37*, 917−920.

(17) Rao, V.; Shashimohan, A. L.; Biswas, A. B. Studies on the Formation of γ-Fe_2O_3 (Maghemite) by Thermal Decomposition of Ferrous Oxalate Dihydrate. *J. Mater. Sci.* **1974**, *9*, 430−433.

(18) Haneda, K.; Morrish, A. H. Magnetite to Maghemite Transformation in Ultrafine Particles. *J. Phys., Colloq.* **1977**, *38*, C1-321−C1-323.

(19) Kim, W.; Suh, C. Y.; Cho, S. W.; Roh, K. M.; Kwon, H.; Song, K.; Shon, I. J. A New Method for the Identification and Quantification of Magnetite-Maghemite Mixture Using Conventional X-Ray Diffraction Technique. *Talanta* **2012**, *94*, 348−352.

(20) Petkov, V.; Cozzoli, P. D.; Buonsanti, R.; Cingolani, R.; Ren, Y. Size, Shape, and Internal Atomic Ordering of Nanocrystals by Atomic Pair Distribution Functions: A Comparative Study of γ-Fe_2O_3 Nanosized Spheres and Tetrapods. *J. Am. Chem. Soc.* **2009**, *131*, 14264−14266.

(21) Can, M. M.; Ozcan, S.; Ceylan, A.; Firat, T. Effect of Milling Time on the Synthesis of Magnetite Nanoparticles by Wet Milling. *Mater. Sci. Eng., B* **2010**, *172*, 72−75.

(22) Yan, H.; Zhang, J.; You, C.; Song, Z.; Yu, B.; Shen, Y. Influences of Different Synthesis Conditions on Properties of Fe_3O_4 Nanoparticles. *Mater. Chem. Phys.* **2009**, *113*, 46−52.

(23) Zheng, Y.-h.; Cheng, Y.; Bao, F.; Wang, Y.-s. Synthesis and Magnetic Properties of Fe_3O_4 Nanoparticles. *Mater. Res. Bull.* **2006**, *41*, 525−529.

(24) Chowdhury, S. R.; Yanful, E. K.; Pratt, A. R. Arsenic Removal from Aqueous Solutions by Mixed Magnetite−Maghemite Nanoparticles. *Environ. Earth Sci.* **2011**, *64*, 411−423.

(25) Kuivila, C. S.; Butt, J. B.; Stair, P. C. Characterization of Surface Species on Iron Synthesis Catalysts by X-Ray Photoelectron Spectroscopy. *Appl. Surf. Sci.* **1988**, *32*, 99−121.

(26) Cannas, C.; Casula, M. F.; Concas, G.; Corrias, A.; Gatteschi, D.; Falqui, A.; Musinu, A.; Sangregorio, C.; Spano, G. Magnetic Properties of γ-Fe_2O_3-SiO_2 Aerogel and Xerogel Nanocomposite Materials. *J. Mater. Chem.* **2001**, *11*, 3180−3187.

(27) Dormann, J. L.; Fiorani, D.; Cherkaoui, R.; Tronc, E.; Lucari, F.; D'Orazio, F.; Spinu, L.; Nogues, M.; Kachkachi, H.; Jolivet, J. P. From Pure Superparamagnetism to Glass Collective State in γ-Fe_2O_3 Nanoparticle Assemblies. *J. Magn. Magn. Mater.* **1999**, *203*, 23−27.

(28) Mikhaylova, M.; Kim, D. K.; Bobrysheva, N.; Osmolowsky, M.; Semenov, V.; Tsakalakos, T.; Muhammed, M. Superparamagnetism of Magnetite Nanoparticles: Dependence on Surface Modification. *Langmuir* **2004**, *20*, 2472−2477.

(29) Santoyo Salazar, J.; Perez, L.; de Abril, O.; Truong Phuoc, L.; Ihiawakrim, D.; Vazquez, M.; Greneche, J.-M.; Begin-Colin, S.; Pourroy, G. Magnetic Iron Oxide Nanoparticles in 10−40 Nm Range: Composition in Terms of Magnetite/Maghemite Ratio and Effect on the Magnetic Properties. *Chem. Mater.* **2011**, *23*, 1379−1386.

(30) Lastovina, T. A.; Bugaev, A. L.; Kubrin, S. P.; Kudryavtsev, E. A.; Soldatov, A. V. Structural Studies of Magnetic Nanoparticles Doped with Rare-Earth Elements. *J. Struct. Chem.* **2016**, *57*, 1444−1449.

(31) Koningsberger, D.; Prins, R. *X-Ray Absorption: Principles, Applications, Techniques of EXAFS, SEXAFS, and XANES*; Wiley: New York, 1988.

(32) Bordiga, S.; Groppo, E.; Agostini, G.; van Bokhoven, J. A.; Lamberti, C. Reactivity of Surface Species in Heterogeneous Catalysts Probed by in Situ X-ray Absorption Techniques. *Chem. Rev.* **2013**, *113*, 1736−1850.

(33) Borfecchia, E.; Lomachenko, K. A.; Giordanino, F.; Falsig, H.; Beato, P.; Soldatov, A. V.; Bordiga, S.; Lamberti, C. Revisiting the Nature of Cu Sites in the Activated Cu-SSZ-13 Catalyst for SCR Reaction. *Chem. Sci.* **2015**, *6*, 548−563.

(34) Lamberti, C.; Prestipino, C.; Bonino, F.; Capello, L.; Bordiga, S.; Spoto, G.; Zecchina, A.; Moreno, S. D.; Cremaschi, B.; Garilli, M.; et al. The Chemistry of the Oxychlorination Catalyst: An in Situ, Time-Resolved XANES Study. *Angew. Chem., Int. Ed.* **2002**, *41*, 2341−2344.

(35) Tulchinsky, Y.; Hendon, C. H.; Lomachenko, K. A.; Borfecchia, E.; Melot, B. C.; Hudson, M. R.; Tarver, J. D.; Korzynski, M. D.; Stubbs, A. W.; Kagan, J. J.; et al. Reversible Capture and Release of Cl₂ and Br₂ with a Redox-Active Metal-Organic Framework. *J. Am. Chem. Soc.* **2017**, *139*, 5992−5997.

(36) Martini, A.; Borfecchia, E.; Lomachenko, K. A.; Pankin, I. A.; Negri, C.; Berlier, G.; Beato, P.; Falsig, H.; Bordiga, S.; Lamberti, C. Composition-Driven Cu-Speciation and Reducibility in Cu-CHA Zeolite Catalysts: A Multivariate XAS/FTIR Approach to Complexity. *Chem. Sci.* **2017**, *8*, 6836−6851.

(37) van Bokhoven, J. A.; Lamberti, C. *X-Ray Absorption and X-Ray Emission Spectroscopy: Theory and Applications*; Wiley: Chichester, 2016.

(38) Filippousi, M.; Angelakeris, M.; Katsikini, M.; Paloura, E.; Efthimiopoulos, I.; Wang, Y.; Zamboulis, D.; Van Tendeloo, G. Surfactant Effects on the Structural and Magnetic Properties of Iron Oxide Nanoparticles. *J. Phys. Chem. C* **2014**, *118*, 16209−16217.

(39) Borfecchia, E.; Mino, L.; Gianolio, D.; Groppo, C.; Malaspina, N.; Martinez-Criado, G.; Sans, J. A.; Poli, S.; Castelli, D.; Lamberti, C. Iron Oxidation State in Garnet from a Subduction Setting: A Micro-XANES and Electron Microprobe ("Flank Method") Comparative Study. *J. Anal. At. Spectrom.* **2012**, *27*, 1725−1733.

(40) Okudera, H.; Yoshiasa, A.; Murai, K.-i.; Okube, M.; Takeda, T.; Kikkawa, S. Local Structure of Magnetite and Maghemite and Chemical Shift in Fe K-Edge XANES. *J. Mineral. Petrol. Sci.* **2012**, *107*, 127−132.

(41) Espinosa, A.; Serrano, A.; Llavona, A.; de la Morena, J. J.; Abuin, M.; Figuerola, A.; Pellegrino, T.; Fernandez, J. F.; Garcia-Hernandez, M.; Castro, G. R.; et al. On the Discrimination Between Magnetite and Maghemite by XANES Measurements in Fluorescence Mode. *Meas. Sci. Technol.* **2012**, *23*, No. 015602.

(42) Corrias, A.; Ennas, G.; Mountjoy, G.; Paschina, G. An X-Ray Absorption Spectroscopy Study of the Fe K Edge in Nanosized Maghemite and in Fe₂O₃−SiO₂ Nanocomposites. *Phys. Chem. Chem. Phys.* **2000**, *2*, 1045−1050.

(43) Corrias, A.; Mountjoy, G.; Loche, D.; Puntes, V.; Falqui, A.; Zanella, M.; Parak, W. J.; Casula, M. F. Identifying Spinel Phases in Nearly Monodisperse Iron Oxide Colloidal Nanocrystal. *J. Phys. Chem. C* **2009**, *113*, 18667−18675.

(44) Sarveena; Vargas, J. M.; Shukla, D. K.; Meneses, C. T.; Mendoza Zelis, P.; Singh, M.; Sharma, S. K. Synthesis, Phase Composition,

Mössbauer and Magnetic Characterization of Iron Oxide Nanoparticles. *Phys. Chem. Chem. Phys.* **2016**, *18*, 9561−9568.

(45) Kataby, G.; Koltypin, Y.; Rothe, J.; Hormes, J.; Felner, I.; Cao, X.; Gedanken, A. The Adsorption of Monolayer Coatings on Iron Nanoparticles: Mössbauer Spectroscopy and XANES Results. *Thin Solid Films* **1998**, *333*, 41−49.

(46) Lastovina, T. A.; Efimova, S. A.; Kudryavtsev, E. A.; Soldatov, A. V. Preparation of the Sm³⁺- Doped Magnetic Nanoparticles via Microwave-Assisted Polyol Synthesis. *Bionanoscience* **2017**, *7*, 4−10.

(47) Lastovina, T. A.; Budnyk, A. P.; Kubrin, S. P.; Soldatov, A. V. Microwave-Assisted Synthesis of Ultra-Small Iron Oxide Nanoparticles for Biomedicine. *Mendeleev Commun.* **2018**, *28*, 167−169.

(48) Langford, J. I.; Wilson, A. J. C. Scherrer After Sixty Years: A Survey and Some New Results in the Determination of Crystallite Size. *J. Appl. Crystallogr.* **1978**, *11*, 102−113.

(49) Pellegrini, R.; Agostini, G.; Groppo, E.; Piovano, A.; Leofanti, G.; Lamberti, C. 0.5 wt.% Pd/C Catalyst for Purification of Terephthalic Acid: Irreversible Deactivation in Industrial Plants. *J. Catal.* **2011**, *280*, 150−160.

(50) Frantti, J.; Fujioka, Y. X-Ray and Neutron Scattering on Disordered Nanosize Clusters: A Case Study of Lead-Zirconate-Titanate Solid Solutions. *Ann. Phys.* **2015**, *527*, 219−237.

(51) Mangold, S.; Steininger, R.; Rolo, T. D.; Gottlicher, J. Full Field Spectroscopic Imaging at the ANKA-XAS- and -SUL-X-Beamlines. *J. Phys.: Conf. Ser.* **2013**, *430*, No. 012130.

(52) Ravel, B.; Newville, M. ATHENA, ARTEMIS, HEPHAESTUS: Data Analysis for X-Ray Absorption Spectroscopy Using IFEFFIT. *J. Synchrotron Radiat.* **2005**, *12*, 537−541.

(53) Matsnev, M. E.; Rusakov, V. S. SpectrRelax: An Application for Mössbauer Spectra Modeling and Fitting. *AIP Conf. Proc.* **2012**, *1489*, 178−185.

(54) Guda, A. A.; Guda, S. A.; Soldatov, M. A.; Lomachenko, K. A.; Bugaev, A. L.; Lamberti, C.; Gawelda, W.; Bressler, C.; Smolentsev, G.; Soldatov, A. V.; et al. Finite Difference Method Accelerated with Sparse Solvers for Structural Analysis of the Metal-Organic Complexes. *J. Phys.: Conf. Ser.* **2016**, *712*, No. 012004.

(55) Guda, S. A.; Guda, A. A.; Soldatov, M. A.; Lomachenko, K. A.; Bugaev, A. L.; Lamberti, C.; Gawelda, W.; Bressler, C.; Smolentsev, G.; Soldatov, A. V.; et al. Optimized Finite Difference Method for the Full-Potential XANES Simulations: Application to Molecular Adsorption Geometries in MOFs and Metal-Ligand Intersystem Crossing Transients. *J. Chem. Theory Comput.* **2015**, *11*, 4512−4521.

(56) Bunău, O.; Joly, Y. Self-Consistent Aspects of X-ray Absorption Calculations. *J. Phys.: Condens. Matter* **2009**, *21*, No. 345501.

(57) de Groot, F.; Vankó, G.; Glatzel, P. The 1s X-Ray Absorption Pre-Edge Structures in Transition Metal Oxides. *J. Phys.: Condens. Matter* **2009**, *21*, No. 104207.

(58) Westre, T. E.; Kennepohl, P.; DeWitt, J. G.; Hedman, B.; Hodgson, K. O.; Solomon, E. I. A Multiplet Analysis of Fe K-Edge 1s → 3d Pre-Edge Features of Iron Complexes. *J. Am. Chem. Soc.* **1997**, *119*, 6297−6314.

(59) Hachani, R.; Lowdell, M.; Birchall, M.; Hervault, A.; Mertz, D.; Begin-Colin, S.; Thanh, N. T. Polyol Synthesis, Functionalisation, and Biocompatibility Studies of Superparamagnetic Iron Oxide Nanoparticles as Potential MRI Contrast Agents. *Nanoscale* **2016**, *8*, 3278−3287.

(60) Lastovina, T. A.; Budnyk, A. P.; Kudryavtsev, E. A.; Nikolsky, A. V.; Kozakov, A. T.; Chumakov, N. K.; Emelyanov, A. V.; Soldatov, A. V. Solvothermal Synthesis of Sm³⁺-Doped Fe₃O₄ Nanoparticles. *Mater. Sci. Eng., C* **2017**, *80*, 110−116.

(61) Bedanta, S.; Kleemann, W. Supermagnetism. *J. Phys. D: Appl. Phys.* **2009**, *42*, No. 013001.

(62) Venkatachalam, A. *Investigations of Some Oxidic and Chalcogenide Spinels*; Lakshmanan, V. I., Ed.; Soc Mining Metallurgy & Exploration Inc.: Salt Lake city, 1990; pp 187−193.

(63) Bødker, F.; Mørup, S. Size Dependence of the Properties of Hematite Nanoparticles. *EPL* **2000**, *52*, 217−223.

(64) Mørup, S.; Topsoe, H. Mossbauer Studies of Thermal Excitations in Magnetically Ordered Microcrystals. *Appl. Phys.* **1976**, *11*, 63−66.

(65) Kündig, W.; Bömmel, H.; Constabaris, G.; Lindquist, R. H. Some Properties of Supported Small α-Fe$_2$O$_3$ Particles Determined with the Mössbauer Effect. *Phys. Rev.* **1966**, *142*, 327−333.

(66) Desautels, R. D.; Skoropata, E.; van Lieropa, J. Moment Fluctuations in 7 nm γ-Fe$_2$O$_3$ Nanoparticles Probed at the Atomic Level Using Mössbauer Spectroscopy. *J. Appl. Phys.* **2008**, *103*, No. 07d512.

(67) Long, G. J.; Grandjean, F. *Mössbauer Spectroscopy Applied to Inorganic Chemistry*; Springer: New York, 1989.

(68) Haneda, K.; Morrish, A. H. Vacancy Ordering in γ-Fe$_2$O$_3$ Small Particles. *Solid State Commun.* **1977**, *22*, 779−782.

(69) Menil, F. Systematic Trends of the ^{57}Fe Mössbauer Isomer Shifts in (FeO$_n$) and (FeF$_n$) Polyhedra. Evidence of a New Correlation Between the Isomer Shift and the Inductive Effect of the Competing Bond *T-X* ($\rightarrow$ Fe) (Where X is O or F and T Any Element with a Formal Positive Charge). *J. Phys. Chem. Solids* **1985**, *46*, 763−789.

(70) Polozhentsev, O. E.; Kubrin, S. P.; Butova, V. V.; Kochkina, V. K.; Soldatov, A. V.; Stashenko, V. V. Structure and Magnetic Properties of Pure and Samarium Doped Magnetite Nanoparticles. *J. Struct. Chem.* **2016**, *57*, 1459−1468.

(71) Bragg, W. H. The Structure of Magnetite and the Spinels. *Nature* **1915**, *95*, 561.

(72) Walz, F. The Verwey Transition - a Topical Review. *J. Phys.: Condens. Matter* **2002**, *14*, R285−R340.

(73) Wright, J. P.; Attfield, J. P.; Radaelli, P. G. Long Range Charge Ordering in Magnetite Below the Verwey Transition. *Phys. Rev. Lett.* **2001**, *87*, No. 266401.

(74) Wright, J. P.; Attfield, J. P.; Radaelli, P. G. Charge Ordered Structure of Magnetite Fe$_3$O$_4$ Below the Verwey Transition. *Phys. Rev. B* **2002**, *66*, No. 214422.

(75) Blasco, J.; Garcia, J.; Subias, G. Structural Transformation in Magnetite Below the Verwey Transition. *Phys. Rev. B* **2011**, *83*, No. 104105.

(76) Goff, R. J.; Wright, J. P.; Attfield, J. P.; Radaelli, P. G. Resonant X-Ray Diffraction Study of the Charge Ordering in Magnetite. *J. Phys.: Condens. Matter* **2005**, *17*, 7633−7642.

(77) Jeng, H. T.; Guo, G. Y.; Huang, D. J. Charge-Orbital Ordering and Verwey Transition in Magnetite. *Phys. Rev. Lett.* **2004**, *93*, No. 156403.

(78) Jeng, H.-T.; Guo, G. Y.; Huang, D. J. Charge-Orbital Ordering in Low-Temperature Structures of Magnetite: GGA+*U* Investigations. *Phys. Rev. B* **2006**, *74*, No. 195115.

(79) Joly, Y.; Lorenzo, J. E.; Nazarenko, E.; Hodeau, J. L.; Mannix, D.; Marin, C. Low-Temperature Structure of Magnetite Studied Using Resonant X-Ray Scattering. *Phys. Rev. B* **2008**, *78*, No. 134110.

(80) Senn, M. S.; Wright, J. P.; Attfield, J. P. Charge Order and Three-Site Distortions in the Verwey Structure of Magnetite. *Nature* **2011**, *481*, 173−176.

(81) Krause, M. O. Atomic Radiative and Radiationless Yields for K-Shells and L-Shells. *J. Phys. Chem. Ref. Data* **1979**, *8*, 307−327.

(82) Bianconi, A.; Dell'Ariccia, M.; Gargano, A.; Natoli, C. R. In *EXAFS and Near Edge Structure*; Bianconi, A.; Inoccia, L.; Stipcich, S., Eds.; Springer-Verlag: Berlin, 1983; pp 57−61.

(83) Carrey, J.; Mehdaoui, B.; Respaud, M. Simple Models for Dynamic Hysteresis Loop Calculations of Magnetic Single-Domain Nanoparticles: Application to Magnetic Hyperthermia Optimization. *J. Appl. Phys.* **2011**, *109*, No. 083921.

(84) Nemati, Z.; Alonso, J.; Martinez, L. M.; Khurshid, H.; Garaio, E.; Garcia, J. A.; Phan, M. H.; Srikanth, H. Enhanced Magnetic Hyperthermia in Iron Oxide Nano-Octopods: Size and Anisotropy Effects. *J. Phys. Chem. C* **2016**, *120*, 8370−8379.

(85) Hiemstra, T. Surface and Mineral Structure of Ferrihydrite. *Geochim. Cosmochim. Acta* **2013**, *105*, 316−325.